RSC Advances

PAPER

View Article Online
View Journal | View Issue



Cite this: *RSC Adv.*, 2018, **8**, 423

# Anti-site defect effect on the electronic structure of a $Bi_2Te_3$ topological insulator

Pei-Yu Chuang,[a] Shu-Hsuan Su,*[a] Cheong-Wei Chong,[a] Yi-Fan Chen,[a] Yu-Heng Chou,[a] Jung-Chun-Andrew Huang,*[abc] Wei-Chuan Chen,[d] Cheng-Maw Cheng,*[d] Ku-Ding Tsuei,[d] Chia-Hsin Wang,[d] Yaw-Wen Yang,[d] Yen-Fa Liao,[d] Shih-Chang Weng,[d] Jyh-Fu Lee,[d] Yi-Kang Lan,[e] Shen-Lin Chang,[f] Chi-Hsuan Lee,[g] Chih-Kai Yang,[g] Hai-Lin Su[h] and Yu-Cheng Wu[h]

Tuning the Fermi level ($E_F$) in $Bi_2Te_3$ topological-insulator (TI) films is demonstrated on controlling the temperature of growth with molecular-beam epitaxy (MBE). Angle-resolved photoemission spectra (ARPES) reveal that $E_F$ of $Bi_2Te_3$ thin films shifts systematically with the growth temperature ($T_g$). The key role that a Bi-on-Te(1) ($Bi_{Te1}$) antisite defect plays in the electronic structure is identified through extended X-ray-absorption fine-structure (EXAFS) spectra at the Bi $L_3$-edge. Calculations of electronic structure support the results of fitting the EXAFS, indicating that the variation of $E_F$ is due to the formation and suppression of $Bi_{Te1}$ that is tunable with the growth temperature. Our findings provide not only insight into the correlation between the defect structure and electronic properties but also a simple route to control the intrinsic topological surface states, which could be useful for applications in TI-based advanced electronic and spintronic devices.

Received 14th August 2017
Accepted 8th December 2017

DOI: 10.1039/c7ra08995c

rsc.li/rsc-advances



## 1. Introduction

Topological insulators (TI) are novel quantum materials with promising applications in advanced spintronic devices. A three-dimensional (3D) TI is a gapped bulk insulator, but possesses gapless conducting surface states.[1,2] These topological surface states in 3D TI arise from a band inversion of the valence and conduction bands due to strong spin–orbit interactions.[3,4] This inversion makes the surface state topologically nontrivial, being protected by the time-reversal symmetry. The surface state in 3D TI shows a helical Dirac-type dispersion, in which the spin is tightly coupled to the momentum, so called spin-momentum locking.[5] $V_2$–$VI_3$-type 3D TIs, such as $Bi_2Se_3$, $Bi_2Te_3$ and $Sb_2Te_3$, have been theoretically predicted and experimentally confirmed.[4,6,7] $Bi_2Te_3$ belongs to the $V_2$–$VI_3$ TI family and has a rhombohedral crystal structure that can be considered to consist of the stacking of –Te(1)–Bi–Te(2)–Bi–Te(1)– quintiple layers (QL).[8] Within a QL unit, the interaction between Bi and Te is a chemical force whereas the interaction between two QL involves a van der Waals force. The surface states of Bi-based TI families are widely regarded as ideal systems for applications in spintronic and quantum devices, but a large bulk charge-carrier contribution generally originates from intrinsic defects, such as anion vacancies and antisite defects in Bi-based TI.[9] When the charge carrier is dominated by bulk donors, the Dirac point (DP) is located deep below the Fermi level, making it difficult to utilize the unique property of the topological surface states. Understanding and manipulating the electronic structure during the growth of a thin film of TI becomes a crucial problem, especially for the effect of key parameters such as the growth temperature on the electronic structure of TI.

For a $Bi_2Te_3$ single crystal near the solid–liquid equilibrium composition for Te ranging from 58 to 62.8 atomic per cent, a substitution of Bi for a Te(1) site ($Bi_{Te1}$) is energetically favored and hole charge carriers dominate. In contrast, electron carriers dominate the behavior in the case of substitution of Te for Bi ($Te_{Bi}$) for Te in a range from 62.8 to 66 atomic per cent. For single-crystalline $Bi_2Te_3$, the p-type and n-type charge-carrier concentration can range from $3 \times 10^{17}$ to $5 \times 10^{19}$ $cm^{-3}$, depending on the initial growth condition with excess either Bi or Te.[10–14] For bulk $Bi_2Te_3$ crystal growth near the solid–liquid

[a]*Department of Physics, National Cheng Kung University, Tainan 701, Taiwan. E-mail: jcahuang@mail.ncku.edu.tw; macg0510@yahoo.com.tw*

[b]*Advanced Optoelectronic Technology Center, National Cheng Kung University, Tainan 701, Taiwan*

[c]*Taiwan Consortium of Emergent Crystalline Materials, Ministry of Science and Technology, Taipei 106, Taiwan*

[d]*National Synchrotron Radiation Research Center, Hsinchu 300, Taiwan. E-mail: makalu@nsrrc.org.tw*

[e]*Materials and Electro-Optic Research Division, National Chung-Shan Institute of Science and Technology, Taoyuan 325, Taiwan*

[f]*Department of Electrophysics, National Chiao Tung University, Hsinchu 300, Taiwan*

[g]*Graduate Institute of Applied Physics, National Chengchi University, Taipei 116, Taiwan*

[h]*School of Materials Science and Engineering, Anhui Provincial Key Laboratory of Advanced Functional Materials and Devices, Hefei University of Technology, Hefei 230009, People's Republic of China*

equilibrium temperature, anti-site defects can be simply described by element compositions. In comparison, thin film growth is far from the equilibrium conditions, so that the composition of Bi/Te can be tuned by growth temperature. In the present work, we report a systematic study of the crystal structure and electronic properties of epitaxial $Bi_2Te_3$ films upon tuning the growth temperature. A correlation between the position of the Dirac point of $Bi_2Te_3$ films *via* angle-resolved photoemission spectra (ARPES) and the coordination number of Bi–$Bi_{Te1}$ *via* extended X-ray-absorption fine structure (EXAFS) spectra is clearly identified. To compare with the experimental results, we conducted a simulation on $Bi_{Te}$ and $Te_{Bi}$ antisite defects with density-functional theory (DFT); the results support the conclusion that the variation of the electronic structure of $Bi_2Te_3$ films is highly correlated with the antisite defects that vary with the growth temperature. Our findings provide also a simple route to manipulate the Dirac point and topological surface states that can yield applications in electronic and spintronic devices.

## 2. Experimental

### 2.1 Sample preparation

The TI films were grown on *c*-plane $Al_2O_3(0001)$ substrates with a MBE system (AdNaNo Corporation, model MBE-9). The sapphire substrates were chemically cleaned with standard procedures before being loaded into the growth chamber. To remove any possible contaminant from the surface, we heated the sapphire substrates to 1000 °C for 1 h under a ultrahigh-vacuum (UHV) environment. Highly pure Bi (99.99%) and Te (99.999%) were evaporated from Knudsen cells; the flux rate was calibrated *in situ* with a quartz crystal microbalance. The base pressure of the MBE system was less than $2 \times 10^{-10}$ Torr; the pressure during growth was kept below $1 \times 10^{-9}$ Torr. The $Bi_2Te_3$ thin films were prepared with a stable beam-flux ratio Te/Bi ($\Phi_{Te/Bi}$) $\sim$ 15; the substrate temperature was varied from 310 °C to 430 °C. The crystallinity of $Bi_2Te_3$ films was monitored *in situ* with reflection high-energy diffraction (RHEED); additional structural characterization was performed with X-ray diffraction (XRD).

### 2.2 XPS and ARPES characterization

The stoichiometry and electronic structure of the $Bi_2Te_3$ films were characterized with X-ray photoemission spectra (XPS) and ARPES. The XPS and ARPES experiments were conducted at beamlines 24A and 21B1 at Taiwan Light Source in National Synchrotron Radiation Research Center. The MBE-grown $Bi_2Te_3$ films with a Te capping layer of thickness $\sim$20 Å were annealed at 260 °C about 1 h in an UHV environment to remove the capping layer before XPS and ARPES measurements. XPS were recorded with an energy analyzer (SPEC Phoiboss150); the core levels of Bi 4f and Te 3d were recorded with photon energy 800 eV. The incident photon energy for XPS measurements was calibrated with Au 4f levels. ARPES were recorded for samples in an UHV chamber equipped with a hemispherical analyzer (Scienta R4000, collection angle $\pm$15°). The ARPES were recorded for samples at 83 K, base pressure $5 \times 10^{-11}$ Torr and photon energy 22 eV; the angular resolution was 0.2° and overall energy resolution was better than 12 meV. The position of the Dirac point was determined from an analysis of momentum distribution curves (MDC).

### 2.3 EXAFS characterization

The local structure of $Bi_2Te_3$ thin films was determined with EXAFS spectra. The $L_3$-edge spectra of Bi (13 419 eV) were recorded near 296 K at beamline 07 A of NSRRC and Taiwan beamline SP12B2 of SPring-8. The fluorescence mode was implemented with the beam incident at 54.7° with respect to the sample plane; the signal was collected with a Lytle detector. The measured energy resolution of the used double-crystal Si(111) monochromator was better than 0.6 eV.

### 2.4 Computational

In this work we used spin-polarized density-functional calculations as implemented in the Vienna *ab initio* simulation package (VASP)[15,16] to derive the electronic band structure. The local-density approximation was selected for the exchange–correlation potential including spin–orbit interaction (SOI). The electron–ion interaction was represented by the projector-augmented wave potential.[17] The cutoff energy for the expansion of wave functions and potentials in the plane-wave basis was chosen to be 300 eV. A $9 \times 9 \times 1$ sampling of *k* points in the first Brillouin zone was adopted. A vacuum space in the supercell was allocated on setting a minimum height 15 Å above the film in the cell, which was proved to be sufficient to minimize artificial interactions between supercells.

## 3. Results and discussion

Fig. 1 depicts the XRD pattern of the MBE-grown $Bi_2Te_3$ films at substrate temperature $T_g$ ranging from 310 °C to 430 °C. For the films grown at lower substrate temperature of $T_g$ = 310 °C, the

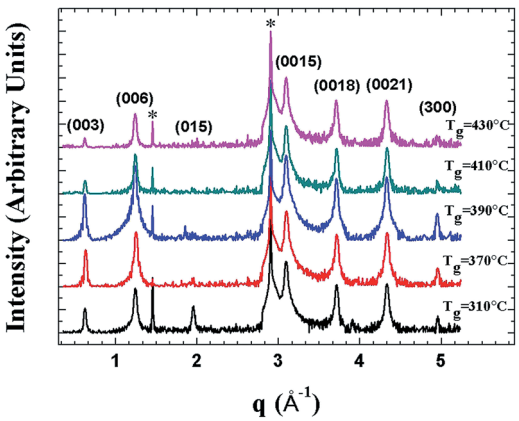


Fig. 1 XRD curves of several $Bi_2Te_3$ epilayers grown with MBE at substrate temperature $T_g$ from 310 to 430 °C. In this $T_g$ range, XRD curves of $Bi_2Te_3$ samples clearly show features related to a single-crystal $Bi_2Te_3$ epilayer that is (0001)-oriented on the sapphire (0001) substrate (indicated by *).

(015) lattice plane that can be attributed to the rhombohedral $Bi_2Te_3$ structure is also observed.[18] The main feature of the XRD patterns of these $Bi_2Te_3$ samples is clearly close to that of $Bi_2Te_3$ (0001) single crystal.

ARPES were measured to probe the quality and electronic structure of MBE-grown $Bi_2Te_3$ films. Fig. 2 shows the band structure recorded along direction $\Gamma$–$K$. In addition to the broad M-shaped valence-band (VB) feature located at binding energy 0.3 eV, a linear band dispersion associated with the topological surface state (TSS) was clearly observed in each sample. ARPES in a series in Fig. 2(a)–(d) show that the Fermi level varied with the growth temperature, $T_g$. At $T_g = 310$ °C, the Dirac point is located at the binding energy ($E_B$) = −0.320 eV; the bottom of the conduction band appears below the Fermi level. On increasing $T_g$ to 370 °C and 390 °C, the position of the Dirac point shifted to $E_B = -0.305$ eV and −0.295 eV, respectively. A similar tendency of the position variation of the Dirac point with increasing $T_g$ below 400 °C was reported by Guang Wang *et al.*,[19] but when $T_g$ was further increased to 410 °C and 430 °C, we observed an opposite trend in which the position of the Dirac point shifted further to $E_B = -0.315$ eV and −0.335 eV, respectively. The ARPES result shows a turning point of the position of the Dirac point that occurred at $T_g \sim 390$ °C. As $E_F$ was located above DP for all samples, the result indicates that the charge carriers of the $Bi_2Te_3$ films were dominantly n-type so that $E_F$ became tunable on varying growth temperature $T_g$.

Hole-dominated carriers with $E_F$ located within the bandgap is expected if the electronic structure were determined mainly by the antisite defects in $Bi_2Te_3$, but the film growth occurred far from the equilibrium growth conditions of a bulk single crystal. The formation of Te vacancies can hence not be avoided during the growth of a $Bi_2Te_3$ film. Te vacancies likely provide n-type carriers as the majority carriers for all $Bi_2Te_3$ films. It is difficult to perform quantitative analysis on the Te vacancies although they play an important role in the electronic structure. Besides point defects in $Bi_2Te_3$, antisite defects, substitutional Bi on Te site ($Bi_{Te}$) or substitutional Te on Bi site ($Te_{Bi}$) are energetically favored.[10,20,21] The tendency of Fermi level shift in the $Bi_2Te_3$ films observed by ARPES suggests the major defects are Te vacancies and/or $Bi_{Te}$. Note that the Te vacancies acts as double donors while the $Bi_{Te}$ as triple acceptors. Therefore, n-type behavior in the $Bi_2Te_3$ films can be attributed to Te vacancies that donate electrons to the conduction band.[22,23] This is consistent with the ARPES observation that the positions of the Fermi level are close to the conduction band. However, the ARPES data show clearly that $E_F$ varies with growth temperature $T_g$, which indicates that antisite defects also play a role in this case. According to the previous reports,[19,24] a shift of the Fermi level in $Bi_2Te_3$ depends strongly on the native point of antisite defects ($Bi_{Te}$ and $Te_{Bi}$) in the Bi–Te compound. Near a stoichiometric $Bi_2Te_3$ with Te fraction about 62.8 at%, acceptor-like $Bi_{Te}$ antisite defects can dominate the carrier behavior. Donor-like $Te_{Bi}$ antisite defects are energetically favored at a larger Te composition, above 63%. The ratio of Bi and Te can be estimated qualitatively from XPS measurements with a peak analysis of the core level spectra of Bi 4f and Te 3d; the secondary electron background is removed with the Shirley background subtraction, as shown in Fig. 3(a) and (b).[25–28]

The tendency that the Fermi level shifted toward the Dirac point in APRES as $T_g$ increased from 310 to 390 °C implies that the concentration of $Bi_{Te}$ antisite defects increased with increasing $T_g$, as shown in Fig. 3(d). The highest Te fraction at 390 °C as revealed in XPS might indicate the diffusion of Te atoms towards the outermost surface. The reduction of Te fraction at $T_g$ >390 °C can be attributed to the desorption of Te from the surface.[29] Nevertheless, a shift of $E_F$ away from the DP at $T_g$ > 390 °C indicates a redistribution of the $Bi_{Te}/Te_{Bi}$ ratio at the elevated growth temperatures. Detailed studies regarding the antisite defects dependent on growth temperature enable a quantitative analysis with EXAFS in the following.

To verify our deductions about the antisite defects, we performed Fourier transformation of the X-ray absorption spectra (XAS) at the Bi-$L_3$ edge; the radial distribution function is shown in Fig. 4(a). The fitted results of extended X-ray-absorption fine-structure (EXAFS) spectra enable a direct identification of the antisite defects in $Bi_2Te_3$ films. In this EXAFS work we took Bi

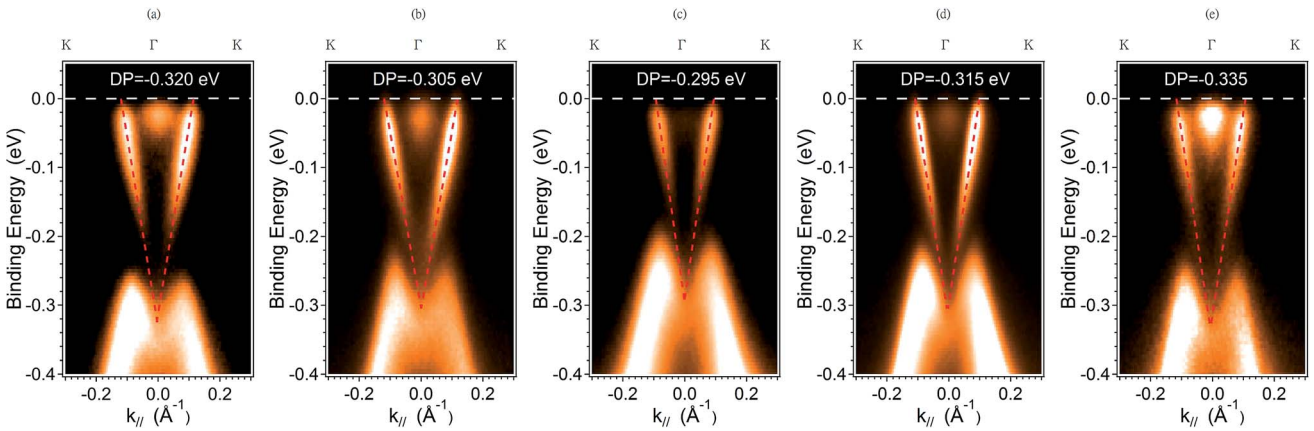


Fig. 2 Band structure of $Bi_2Te_3$ at various $T_g$: (a) 310 °C (DP = −0.32 eV). (b) 370 °C (DP = −0.305 eV). (c) 390 °C (DP = −0.295 eV). (d) 410 °C (DP = −0.315 eV). (e) 430 °C (DP = −0.335 eV). All spectra were recorded along the $\Gamma$–$K$ direction. The panels show the ARPES intensity maps. The surface states, valence band and conduction band of the bulk states are denoted SS, VB and CB, respectively.

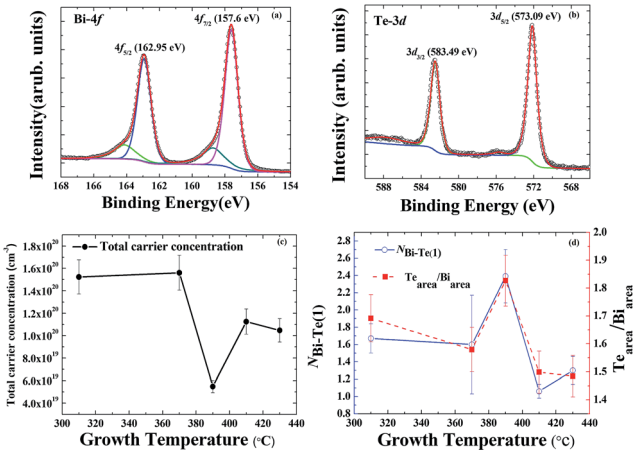


Fig. 3 XPS of (a) Bi-4f core-level spectra and (b) Te-3d core-level spectra of the $Bi_2Te_3$ thin film grown at 390 °C. (c) Total carrier concentration of the $Bi_2Te_3$ films as a function of the growth temperature measured by Hall measurement. (d) The Te/Bi ratio of the $Bi_2Te_3$ thin films as a function of the growth temperature.

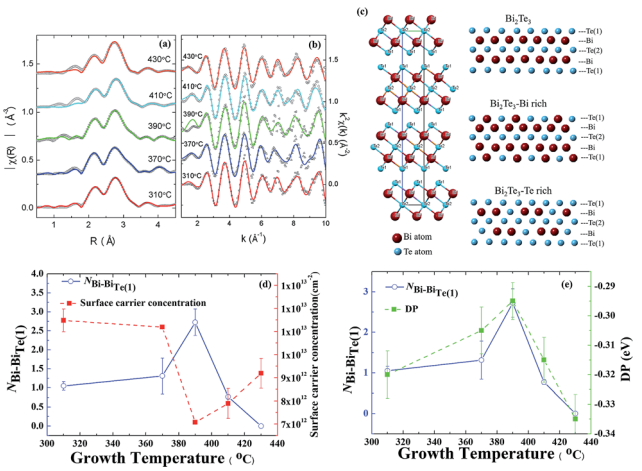


Fig. 4 EXAFS spectra at the Bi $L_3$-edge of the $Bi_2Te_3$ thin films. The curves are vertically shifted for the substrate temperature. (a) Fourier transform of the *R*-space (symbols) together with the theoretical fit to the first shells (solid line). (b) *k*-Space (symbols) together with the best fit (solid line). (c) Hexagonal conventional unit cells of $Bi_2Te_3$; schematic diagram of one QL of the mechanism of the antisite defect in Bi-rich and Te-rich conditions, respectively. (d) $Bi_{Te}$ antisite of Bi–Bi averaged coordination number and surface carrier concentration (estimated from the Fermi level crossing $k_F$) plotted *versus* $T_g$. (e) $Bi_{Te}$ antisite of Bi–Bi averaged coordination number and Dirac point at binding energy plotted *versus* $T_g$.

instead of Te as the central atom, because the two Te sites in each unit cell make the analysis difficult. Herein, EXAFS spectra were recorded with the background subtraction of the XAS data $\mu(E)$ and conversion of $\mu(E)$ to $\chi(k)$; both processes were performed with ATHENA using the IFEFFIT XAS package.[30] The Fourier transforms (FT) of *k*-weighted EXAFS spectra use Hann windows with *k* ranging from 1.2 to 10 $Å^{-1}$, as shown in Fig. 4(b). The rhombohedral primitive and hexagonal unit cell of $Bi_2Te_3$ consists of a five-layer lamellar structure of one quintuple layer (QL). The schematic diagram in Fig. 4(c) shows that a –Te(1)–Bi–Te(2)–Bi–Te(1)– five-layer structure; one Bi atom coordinates three Te atoms at each Te site. According to calculations that provided predictions for the Bi-rich condition, $Bi_{Te1}$ has the least formation energy, 0.4 eV and 0.9 eV, which is less than for $Bi_{Te2}$ and $Te_{Bi}$, respectively. For a Te-rich condition, $Te_{Bi}$ has the least formation energy, 0.7 eV and 1.1 eV, which is less than for $Bi_{Te1}$ and $Bi_{Te2}$, respectively.[23] The coordination relevant for Bi and Te(1) and the bond length of quantitative analysis is indicated in Table 1. At growth temperatures $T_g$ = 310, 370 and 390 °C, the coordination numbers of Bi–$Bi_{Te1}$ ($N_{Bi-BiTe1}$) that correspond to the substitution of Bi for Te(1) are 1.05 ± 0.11, 1.312 ± 0.47 and 2.725 ± 0.35, respectively. Accordingly, the length of the Bi–Te(1) bond decreased to 3.04 ± 0.31 Å, 3.02 ± 1.07 Å, and 2.88 ± 0.37 Å, as more Te(1) sites became occupied with Bi atoms. When the growth temperature exceeded 390 °C, the coordination number of Bi–$Bi_{Te1}$ ($N_{Bi-BiTe1}$) decreased to 0.77 ± 0.06 at $T_g$ = 410 °C. Moreover, no Bi substitution was observed at $T_g$ = 430 °C. The length of the Bi–Te(1) bond increased to 3.06 ± 0.23 Å and 3.04 ± 0.36 Å at $T_g$ = 410 and 430 °C respectively.

On increasing growth temperature $T_g$ to 390 °C, the fitted results of EXAFS clearly show the substitution of a Te(1) site by a Bi atom with increased coordination number of Bi–$Bi_{Te1}$. Because of the extra holes created from antisite $Bi_{Te}$, a smaller Fermi level crossing $k_F$ was observed from ARPES,[31] indicating a decreased concentration of electron carriers. For a growth temperature above $T_g$ = 390 °C, the coordination number of Bi–$Bi_{Te1}$ decreased, accompanied with an incremented concentration of electron carriers as shown in Fig. 4(d). The evolution of the DP ($E_F$) as a function of growth temperature $T_g$ exhibits a trend similar to that of the coordination number of Bi–$Bi_{Te1}$, as displayed in Fig. 4(e). Both the $T_g$-dependent DP and Bi–$Bi_{Te1}$ coincide with the variation in the concentration of electron carriers.

To confirm the above experimental studies and analyses, we calculated the electronic band structure of $Bi_2Te_3$ considering varied chemical composition. Four quintuple layers of pristine $Bi_2Te_3$ were used; one Te in the structure was replaced with a Bi atom and *vice versa*. The concentration of Bi was increased from 40% to 41.7% ($Bi_{23}Te_{37}$) in the former case and decreased from 40% to 38.3% in the latter. Drawn in Fig. 5(a) is the band structure of the pristine $Bi_2Te_3$ with red circles representing the contribution of the surface states of $Bi_2Te_3$. Fig. 5(b) shows the

Table 1 Rhombohedral primitive of first-shell EXAFS fitted results for $Bi_2Te_3$ TI thin films. $N_{Bi-Te1}$ is the Bi–Te(1) average coordination number, $BL_{Bi-Te1}$ is the Bi–Te(1) bond length, and $N_{Bi-BiTe1}$ is the $Bi_{Te}$ antisite of the Bi–Bi average coordination number, $BL_{Bi-BiTe1}$ is the $Bi_{Te}$ antisite of the Bi–Bi bond length

| Sample | $N_{Bi-Te1}$ | $BL_{Bi-Te1}$ (Å) | $N_{Bi-BiTe1}$ | $BL_{Bi-BiTe1}$ (Å) |
|---|---|---|---|---|
| $T_g$ = 310 °C | 1.67 ± 0.17 | 3.04 ± 0.31 | 1.05 ± 0.11 | 3.13 ± 0.32 |
| $T_g$ = 370 °C | 1.6 ± 0.57 | 3.02 ± 1.07 | 1.312 ± 0.47 | 3.11 ± 1.1 |
| $T_g$ = 390 °C | 2.39 ± 0.31 | 2.88 ± 0.37 | 2.725 ± 0.35 | 3.11 ± 0.4 |
| $T_g$ = 410 °C | 1.06 ± 0.08 | 3.06 ± 0.23 | 0.77 ± 0.06 | 3.17 ± 0.24 |
| $T_g$ = 430 °C | 1.3 ± 0.16 | 3.04 ± 0.36 | None | None |

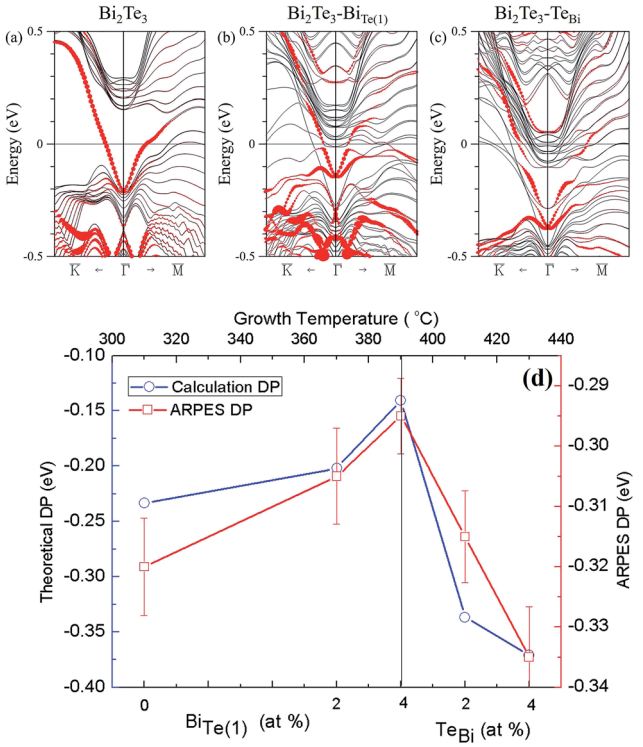


Fig. 5 Band structure of $Bi_2Te_3$ from calculations of electronic structure for Bi-rich and Te-rich conditions. The direct coordinates of high symmetry points in the Brillouin zone are *K*, *Γ* and *M* as the Dirac point of $Bi_2Te_3$. (a) Electronic structure of four quintuple layers of pristine $Bi_2Te_3$ near the *Γ* point. The band structure is shown with (b) replacement of one Bi atom with a Te atom and (c) replacement of one Te atom with a Bi atom in 4 QL $Bi_2Te_3$. The size of the red circle indicates a contribution of the surface state in the low-energy band structure. (d) Theoretical Dirac points with Bi-rich and Te-rich antisite defect concentrations are compared with the ARPES-measured Dirac points.

energy bands for the Bi-rich structure, with its Dirac point shifting upward in energy. In Fig. 5(c), however, the Dirac point in the Te-rich structure shifts downward in energy. The calculated energy-band structures are consistent with the $T_g$-dependent DP ($E_F$) and Bi–$Bi_{Te1}$. As Fig. 5(d) shows, the formation of Bi–Te(1) produces a shift of the $E_F$ towards the maximum of valence band. With decreased substitution of Bi in Te(1), $Te_{Bi}$ became the dominant defects, resulting in an increased concentration of electron carriers so that the $E_F$ shifted away from the maximum of valence band.

## 4. Conclusions

On controlling the growth temperature using a MBE method, we fabricated $Bi_2Te_3$ TI thin films with a varied Fermi level. ARPES and EXAFS results reveal direct evidence for the substitution of Bi for the Te(1) site, which is the key origin for the shift of the Fermi level or the position of the Dirac point in $Bi_2Te_3$. Calculations of the electronic structure support these experiments. The calculated structure of the energy band that took into account the existence of $Bi_{Te}$ and $Te_{Bi}$ antisite defects with Bi-rich and Te-rich conditions further revealed that the variation of the electronic structure in $Bi_2Te_3$ films can be attributed to the antisite defects that are tunable with the growth temperature. Our approaches and results demonstrated the growth of homogenous n-type $Bi_2Te_3$ films, showing the potential for topological insulator-based device applications.

## Author contributions

S. H. Su, C. W. Chong and J. C. A. Huang designed and prepared the experiment. P. Y. Chuang, W. C. Chen, C.-M. Cheng and K.-D. Tsuei performed ARPES measurements. The thin-film growth was performed by Y. F. Chen, Y. H. Chou, and P. Y. Chuang, for C.-H. Wang, Y. F. Liao, S. C. Weng, J. F. Lee, and Y.-W. Yang characterized samples with XPS and EXAFS. Y. K. Lan, S. L. Chang, C. H. Lee, C. K. Yang provided theoretical support. All authors have given approval to the final version of the manuscript.

## Conflicts of interest

There are no conflicts to declare.

## Acknowledgements

Ministry of Science and Technology Republic of China, Taiwan supported this research under contract MOST 103-2119-M-006-015 and 105-2112-M-213-006-MY2. Funding was received also from the headquarters of University Advancement at NCKU, which is sponsored by the Ministry of Education, Taiwan ROC. The National Synchrotron Radiation Research Center (NSRRC) is operated under the Ministry of Science and Technology of Taiwan.

## References

1 J. E. Moore, *Nature*, 2010, **464**, 194–198.
2 X.-L. Qi and S.-C. Zhang, *Rev. Mod. Phys.*, 2011, **83**, 1057–1110.
3 B. A. Bernevig, T. L. Hughes and S.-C. Zhang, *Science*, 2006, **314**, 1757–1761.
4 H. Zhang, C.-X. Liu, X.-L. Qi, X. Dai, Z. Fang and S.-C. Zhang, *Nat. Phys.*, 2009, **5**, 438–442.
5 M. Z. Hasan and C. L. Kane, *Rev. Mod. Phys.*, 2010, **82**, 3045–3067.
6 Y. Xia, D. Qian, D. Hsieh, L. Wray, A. Pal, H. Lin, A. Bansil, D. Grauer, Y. S. Hor, R. J. Cava and M. Z. Hasan, *Nat. Phys.*, 2009, **5**, 398–402.
7 Y. L. Chen, J. G. Analytis, J.-H. Chu, Z. K. Liu, S. K. Mo, X. L. Qi, H. J. Zhang, D. H. Lu, X. Dai, Z. Fang, S. C. Zhang, I. R. Fisher, Z. Hussain and Z.-X. Shen, *Science*, 2009, **325**, 178–181.
8 A. Mzerd, D. Sayah, J. C. Tedenac and A. Boyer, *J. Cryst. Growth*, 1994, **140**, 365–369.
9 D. Hsieh, Y. Xia, D. Qian, L. Wray, J. H. Dil, F. Meier, J. Osterwalder, L. Patthey, J. G. Checkelsky, N. P. Ong, A. V. Fedorov, H. Lin, A. Bansil, D. Grauer, Y. S. Hor, R. J. Cava and M. Z. Hasan, *Nature*, 2009, **460**, 1101–1105.

10 G. R. Miller and C.-Y. Li, *J. Phys. Chem. Solids*, 1965, **26**, 173–177.
11 R. F. Brebrick, *J. Phys. Chem. Solids*, 1969, **30**, 719–731.
12 C. B. Satterthwaite and R. W. Ure Jr, *Phys. Rev.*, 1957, **108**, 1164–1170.
13 H. Zou, D. M. Rowe and G. Min, *J. Cryst. Growth*, 2001, **222**, 82–87.
14 H. Zou, D. M. Rowe and S. G. K. Williams, *Thin Solid Films*, 2002, **408**, 270–274.
15 G. Kresse and J. Hafner, *Phys. Rev. B: Condens. Matter Mater. Phys.*, 1993, **48**, 13115–13118.
16 G. Kresse and J. Furthmiiller, *Comput. Mater. Sci.*, 1996, **6**, 15–50.
17 G. Kresse and D. Joubert, *Phys. Rev. B: Condens. Matter Mater. Phys.*, 1999, **59**, 1758–1775.
18 D. H. Kim, E. Byon, G. H. Lee and S. Cho, *Thin Solid Films*, 2006, **510**, 148–153.
19 G. Wang, X.-G. Zhu, Y.-Y. Sun, Y.-Y. Li, T. Zhang, J. Wen, X. Chen, K. He, L.-L. Wang, X.-C. Ma, J.-F. Jia, S. B. Zhang and Q.-K. Xue, *Adv. Mater.*, 2011, **23**, 2929–2932.
20 A. Hashibon and C. Elsässer, *Phys. Rev. B: Condens. Matter Mater. Phys.*, 2011, **84**, 144117.
21 D. O. Scanlon, P. D. C. King, R. P. Singh, A. de la Torre, S. McKeown Walker, G. Balakrishnan, F. Baumberger and C. R. A. Catlow, *Adv. Mater.*, 2012, **24**, 2154–2158.
22 P. Pecheur and G. Toussaint, *J. Phys. Chem. Solids*, 1994, **55**(4), 327–338.
23 S. X. Zhang, L. Yan, J. Qi, M. Zhuo, Y.-Q. Wang, R. P. Prasankumar, Q. X. Jia and S. T. Picraux, *Thin Solid Films*, 2012, **520**, 6459–6462.
24 S. Cho, Y. Kim, A. DiVenere, G. K. Wong and J. B. Ketterson, *Appl. Phys. Lett.*, 1999, **75**, 1401–1403.
25 D. A. Shirley, *Phys. Rev. B: Solid State*, 1972, **5**, 4709–4714.
26 M. C. Burrell and N. R. Armstrong, *Appl. Surf. Sci.*, 1983, **17**, 53–69.
27 H. E. Bishop, *Surf. Interface Anal.*, 1981, **3**, 272–274.
28 S. Tougaard, *J. Electron Spectrosc. Relat. Phenom.*, 1999, **52**, 243–271.
29 K. Schouteden, K. Govaerts, J. Debehets, U. Thupakula, T. Chen, Z. Li, A. Netsou, F. Song, D. Lamoen, C. V. Haesendonck, B. Partoens and K. Park, *ACS Nano*, 2016, **10**(9), 8778–8787.
30 B. Ravel and M. Newville, *J. Synchrotron Radiat.*, 2005, **12**, 537–541.
31 C. W. Luo, H. J. Wang, S. A. Ku, H.-J. Chen, T. T. Yeh, J.-Y. Lin, K. H. Wu, J. Y. Juang, B. L. Young, T. Kobayashi, C.-M. Cheng, C.-H. Chen, K.-D. Tsuei, R. Sankar, F. C. Chou, K. A. Kokh, O. E. Tereshchenko, E. V. Chulkov, Y. M. Andreev and G. D. Gu, *Nano Lett.*, 2013, 5797–5802.